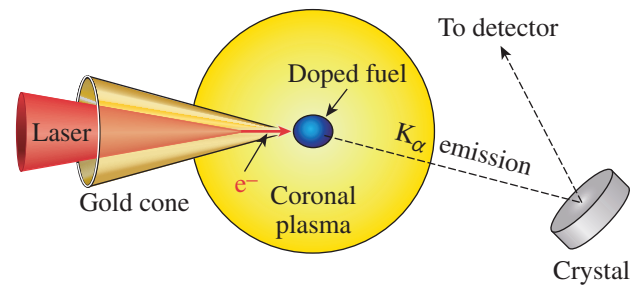


Characterization of a High-Photon-Energy X-Ray Imager

Introduction

In the *fast-ignition* (FI) approach to inertial confinement fusion (ICF), a compressed deuterium–tritium (DT) fuel capsule is ignited by injecting high-energy particles just prior to peak compression.¹ In the cone-in-shell concept, the particles are energetic (*fast*) electrons that are accelerated from the tip of a cone by a high-energy, short-pulse laser with a power of several petawatts. The hollow cone is embedded in a capsule that is imploded by a high-energy nanosecond laser with energies of several hundred kilojoules. The cone-in-shell concept reduces the distance over which the electrons must propagate to reach the compressed part of the fuel while maintaining a plasma-free path for the short-pulse ignitor laser. Experiments that determine the fast-electron penetration efficiency into FI fuel capsules are essential. Surrogate integrated experiments² were performed on the 60-beam OMEGA Laser System³ to assess the fast-electron coupling from a measurement of the neutron-yield enhancement from compressed deuterated plastic shells. Those experiments allow only a global coupling efficiency to be inferred. They did not show where the fast electrons deposited their energy in the compressed plastic. Imaging K_α emission generated by fast electrons while propagating through a buried fluorescent layer is a powerful technique to determine local energy deposition.⁴ In integrated experiments, this technique has been further developed by imaging the K_α x rays emitted from fluorescent materials that are doped into the fuel.^{5,6} Figure 136.5 illustrates this concept. Electrons accelerated from the cone tip propagate into the compressed capsule where they stimulate the emission of K_α , which propagates out of the capsule. A spherically bent crystal, oriented at the Bragg angle, collects and focuses the K_α photons to an x-ray detector [charge-coupled device (CCD) or imaging plate]. The resulting image shows the spatial distribution of the K_α photons from which the spatial distribution of the fast electrons can be inferred.

The use of K_α emission in ICF studies is well established, with most applications employing the $K_{\alpha 1}$ of Cu at ~ 8.048 keV. The fast-electron spreading angle in flat-foil targets, irradiated with a high-intensity laser, is routinely inferred by imaging the



E21813JR

Figure 136.5

Fast electrons, originating from the tip of a gold cone inserted into an ICF capsule, propagate into the doped fuel, where they stimulate the emission of K_α x rays. The x rays, which are imaged to a detector using a spherically bent crystal, are used to infer the fast-electron spatial distribution.

$K_{\alpha 1}$ emitted from Cu layers buried at different depths inside the foil.⁴ Another application involves backlighting the ICF fuel assembly with Cu $K_{\alpha 1}$ to generate radiographic information about the fuel density.⁷ The use of Cu $K_{\alpha 1}$ to diagnose the penetration efficiency of fast electrons in hot dense ICF fuel capsules is limited, however, by the K_α line shift that accompanies high-temperature–induced ionization in the background fuel.⁵ As the K_α lines shift in energy, they move outside the acceptance bandwidth of the imaging crystals; consequently, the detection efficiency drops. For Cu $K_{\alpha 1}$, a background temperature of ~ 35 eV is sufficient for the center wavelength to shift beyond the acceptance bandwidth of a typical quartz crystal reflector cut with Miller indices (211) (Ref. 8). One-dimensional hydrodynamic calculations performed to estimate the temperature of a $870\text{-}\mu\text{m}$ -diam fuel capsule with a $40\text{-}\mu\text{m}$ -thick shell, imploded using 20 kJ from the OMEGA laser, indicated a shell temperature in excess of 200 eV (Ref. 9).

The issue of line shifting may be mitigated by using K_α radiation from higher-Z materials, such as Zr, that are more robust against temperature-induced shifts. Promising results with a novel quartz-crystal imager working at a photon energy of 15.6909 keV, corresponding to the Zr $K_{\alpha 2}$ line, were recently reported.¹⁰ Calculations described in Ref. 10 suggest that the center wavelength of the Zr $K_{\alpha 2}$ line remains inside

the acceptance band of a quartz reflector up to a temperature of at least 200 eV. There is very little experimental work reporting on crystal imaging systems at such high photon energies. This article reports on the performance of a spherically curved quartz-crystal imager designed to reflect photons with an energy of 15.6909 keV. Since the design of the imaging system relies on an accurate knowledge of the crystal, which is cut with Miller indices (234), measurements were taken to determine the Bragg angle, rocking curve, peak reflectivity, and integrated reflectivity. Several curved crystals and a flat sample were characterized using a narrow-bandwidth x-ray source tuned to 15.6909 keV. The imager was successfully tested using a Zr plasma source generated with a 10-J, 1-ps laser system. The measured peak reflectivity from the laser experiment is in agreement with the results from a synchrotron facility.

Quartz-Crystal Imager

Figure 136.6 shows the configuration in which the K_{α} imager is aligned for use in laser–solid experiments. In the first stage of alignment, a continuous-wave (cw) alignment laser is propagated through target chamber center (TCC), indicated by the position of the imaging fiducial in Fig. 136.6, and onto the center of the crystal. To enhance its reflectivity in the visible, the crystal is coated with 30 nm of Al. The crystal is oriented to reflect the laser light back along its own path. This arrangement defines the origin of the angular coordinate system. The crystal is then rotated through an angle $\theta_{1/2}$, where $\theta_{1/2}$ is $90^{\circ} - \theta_B$ and θ_B is the Bragg angle for the K_{α} diffraction. The laser light is then reflected through a full angle $\theta_F = 2\theta_{1/2}$.

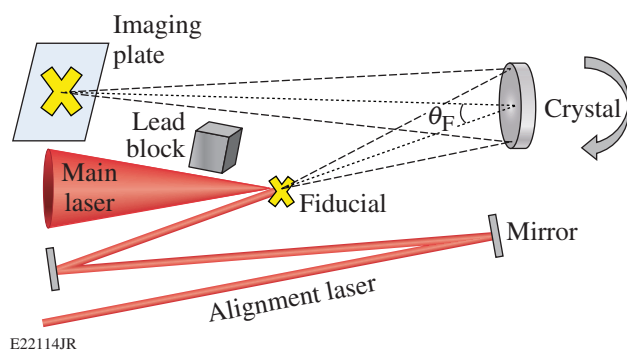


Figure 136.6

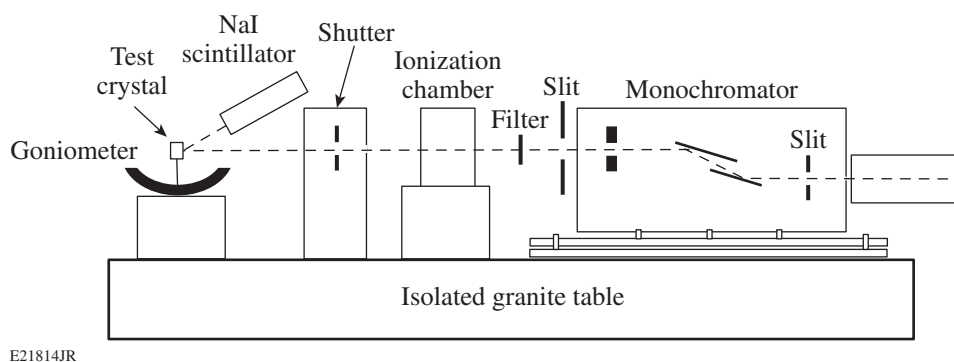
Schematic representation of a K_{α} x-ray imager simultaneously demonstrating the alignment and experimental configurations. For the experiment with the main laser, the curved crystal is rotated to satisfy the Bragg condition for K_{α} x rays that are diffracted and focused onto the imaging plate.

The fiducial is then positioned at TCC and imaged to an imaging plate (or CCD camera) with a magnification m that is determined by the crystal focal length f and the fiducial–crystal

separation distance s_0 by $m = f/(s_0 - f)$. The position of the visible image is recorded. In the experiment, with the fiducial and alignment laser removed, the main laser irradiates a target placed at TCC and the K_{α} emission is imaged onto the imaging plate with the same magnification. The imaging plate is wrapped in Al foil to prevent exposure to room and laser light. A lead block placed between the target and the imaging plate prevents the direct line-of-sight x-ray irradiation of the imaging plate. The alignment technique relies on the visible and K_{α} images being close to coincident. If the visible image forms at an angle that is outside the crystal's rocking-curve range of angles, the Bragg condition will not be satisfied for the K_{α} emission and no K_{α} image will form. Such a discrepancy arises from misalignment of the crystal planes and the crystal surface. In the laser–solid experiments described below, a fiducial was imaged by the crystal designated Sph3 using visible light from the alignment laser before being rotated to the correct position for K_{α} diffraction with an accuracy of 0.01° . The displacement between the visible and the K_{α} images along the dispersion direction 1.85 m away at the imaging plate was ~ 2 mm, corresponding to an angular offset of $\sim 0.06^{\circ}$. In this case, the offset was within the measured rocking-curve width of 0.12° full width at half maximum (FWHM) of this crystal. In general, the visible image can be offset by a predetermined angle to ensure the Bragg condition is satisfied for the K_{α} emission.

Determination of the Crystal Bragg Angle, Rocking Curve, and Reflectivity

Measurements were made to determine the Bragg angle, rocking curve, and reflection efficiency of three curved (25-cm focal length) and one flat sample of a quartz crystal (Miller indices 234) for a photon energy of 15.6909 keV corresponding to the $K_{\alpha 2}$ line of Zr. The measurements were made with the X15A x-ray beamline at the National Synchrotron Light Source at Brookhaven National Laboratory. Figure 136.7 shows the experimental configuration. The X15A beamline provides x rays from around $E_{\nu} = 5$ keV to $E_{\nu} = 28$ keV. A slit ensures that the x rays are collimated. A quartz-crystal monochromator selects the energy, providing a beam with a bandwidth $\Delta E/E \sim 10^{-4}$. The monochromator crystals are cut perpendicular to the axis with Miller indices (111) corresponding to a lattice spacing of 3.136 \AA . The crystal surfaces are set to be parallel and are rotated together to select a specific energy. The monochromator was first calibrated using the K edge of Zr at $E = 17.998$ keV, corresponding to an x-ray angle of incidence from the storage ring of 6.3057° . The monochromator crystals were then rotated to select the desired x-ray energy of $E = 15.6909$ keV corresponding to Zr $K_{\alpha 2}$. In addition to the selected energy, the monochromator passes x rays whose energy corresponds



E21814JR

Figure 136.7

Experimental configuration. A monochromator selects x rays with a bandwidth of $\Delta E/E = 10^{-4}$. The beam is apertured to 1.6 mm (horizontally) by 100 μm (vertically). An ionization chamber measures the flux. The crystal is mounted on a motorized goniometer that rotates the crystal in the vertical direction. A shutter, synchronized with the goniometer, releases the beam when the crystal is stationary. Photons reflected from the crystal are detected using a NaI scintillator.

to the third, fourth, and fifth higher harmonic orders.¹¹ The flux of these x rays is sequentially weaker. At 15.6909 keV, the fundamental carries 99.7% of the x-ray energy while the third, fourth, and fifth orders contribute 0.28%, 0.013%, and 0.0003% of the energy, respectively. Filtering of the x-ray beam, a necessity for the experiment described here, increases the relative amount of higher-order x rays through differential attenuation. To suppress the propagation of higher orders of the fundamental x-ray energy, the monochromator was slightly detuned from the peak transmission angle of its rocking curve to the 50% transmission angle. With such a configuration, the third-order component is reduced by a factor of ~ 100 , while the higher-order components are suppressed even more.

To limit the overall flux, a second lead slit apertured the x-ray beam to 1.6 mm \times 100 μm in the horizontal and vertical directions, respectively. Mo filter foils can be placed in front of the slit to further attenuate the beam where necessary. An ionization chamber measures the x-ray flux after the slit. The x-ray flux at the ionization chamber is directly proportional to the electron current in the main storage ring. A computer-controlled shutter sets the x-ray exposure time. Typical exposure times were 1 s with an absolute error of ~ 20 ms. The test crystal is mounted on a computer-controlled goniometer with a 90° full range of motion. X rays reflected from the crystal were measured using a NaI scintillator positioned to intercept the x rays at the focus of the curved crystal. The test crystal was positioned to intercept the x-ray beam at its center. To obtain the rocking curve, the goniometer rotated the test crystal about its center in 0.0025° steps in the vertical direction. For each step, the rotation paused and the shutter opened for 1.0 s. The large NaI detector with a radius of 2.54 cm ensured that all the reflected x-ray photons were collected over the entire angular

range. The same procedure was used for all four samples. Three crystals (flat, Sph1, and Sph2) were provided by Inrad Optics and were fabricated from the same batch, while the curved crystal Sph3 was provided by Eco Pulse. The Inrad crystals had a thickness of 71 ± 1 μm and a diameter of 30 mm, while the Eco Pulse crystal had a thickness of 125 μm and a diameter of 25 mm. To determine the energy incident on the crystal, the scintillator was placed in front of the crystal to directly intercept the x-ray beam at normal incidence. To reduce the x-ray signal below the scintillator saturation level, a 225- μm -thick Mo filter was placed (as indicated in Fig. 136.7) to attenuate the beam.

Prior to obtaining its efficiency with the NaI scintillator, the Bragg angle of Sph3 was measured using a Fuji SR imaging-plate detector. The imaging plate was oriented in the vertical direction and positioned in place of the scintillator. To prevent room-light illumination of the imaging plates, they were wrapped in a 25- μm -thick sheet of Al foil. The crystal was first aligned in its mount on an optical table and oriented such that a horizontally propagating cw laser, with normal incidence on the crystal, was back-reflected along its own path. The crystal and mount were then transferred to the goniometer and swept through an angular range of 4°. The Bragg angle is computed by determining the vertical position of the peak of the rocking curve, recorded on the imaging plate, relative to the x-ray beam and the distance of the peak position to the center of the crystal. Averaging over four sweeps, the peak was observed to occur at an incidence angle of $\theta_{1/2} = 2.80^\circ$ with a standard deviation of 0.06°. The variation arises from the finite repeatability of repositioning the imaging plate between measurements. A further error associated with the finite precision with which the relevant distances could be measured was evaluated to be

$\sim \pm 0.25^\circ$. The Bragg angle was therefore measured to be $\theta_B = 87.2 \pm 0.3^\circ$ for the Zr $K_{\alpha 2}$ line (15.6909 keV), which results in an inferred crystal $2d$ spacing of $2d = 1.5822(4) \text{ \AA}$ using Bragg's law ($n\lambda = 2d\sin\theta_B$) in the second order. In addition, Inrad provided rocking-curve measurements for their samples using the Cu $K_{\alpha 1}$ line at 8.0478 keV and measured a Bragg peak at $(76.75 \pm 0.10)^\circ$ in the first order, from which $2d = 1.5827(7) \text{ \AA}$ is inferred. The corresponding Bragg angle in the second order for the Zr $K_{\alpha 2}$ line is $(86.8 \pm 0.5)^\circ$. Both inferred $2d$ values agree within the measurement uncertainty and are close to the calculated value of $2d_{\text{cal}} = 1.5825 \text{ \AA}$ (Ref. 6).

The rocking curves and reflection efficiencies for all four crystals are shown in Fig. 136.8. The results show that the spherical crystal Sph1 had the highest reflectivity of the curved crystals at around $(3.6 \pm 0.7) \times 10^{-4}$ with a curve FWHM of $\sim 0.09^\circ$. The primary errors in the reflectivity measurement arise from jitter in the scintillator exposure time as a result of the shutter response and from the uncertainty in the thickness of the Mo stack used to filter the direct beam. For the exposure time employed, the shutter error is estimated to be $\sim 2\%$. The stack thickness was calculated from the total weight, measured using a Scientech analytical balance, and the stack transverse size, measured with digital calipers. The associated error in the transmission was determined to be around $\sim 17\%$. Errors associated with uncertainties in the storage ring current, the

free-space x-ray propagation distances, and photon-counting statistics in the scintillator are negligible. A flat crystal from the same production batch produced a very similar result, showing that the crystal bending had a minor effect on the rocking curve. A lower reflectivity was measured for Sph2 from the same production batch, while the sample Sph3 had an $\sim 4\times$ -lower peak reflectivity. The results are summarized in Table 136.I. As a check, the measurements were repeated with Fujifilm SR imaging-plate detectors, instead of the NaI scintillator, producing similar results, albeit with larger errors. The SR imaging-plate detectors were also used to determine the homogeneity of the reflectivity of crystal Sph3 over a region of its surface. The crystal was translated to positions $\pm 5 \text{ mm}$ above, below, and to the side of the center position, and the measurements were repeated with no significant variation in the performance at the different sites.

Table 136.I: Rocking-curve width, peak reflectivity, and integrated reflectivity of a flat and various curved quartz (234) crystals at the Zr $K_{\alpha 2}$ line (15.6909 keV).

Crystal	FWHM (θ°)	Peak reflectivity	Integrated reflectivity (mrad)
Flat	0.11	$(3.7 \pm 0.7) \times 10^{-4}$	$(8.8 \pm 1.8) \times 10^{-4}$
Sph1	0.09	$(3.6 \pm 0.7) \times 10^{-4}$	$(7.7 \pm 1.8) \times 10^{-4}$
Sph2	0.14	$(2.9 \pm 0.6) \times 10^{-4}$	$(7.0 \pm 1.4) \times 10^{-4}$
Sph3	0.12	$(9.0 \pm 1.8) \times 10^{-5}$	$(2.5 \pm 0.6) \times 10^{-4}$

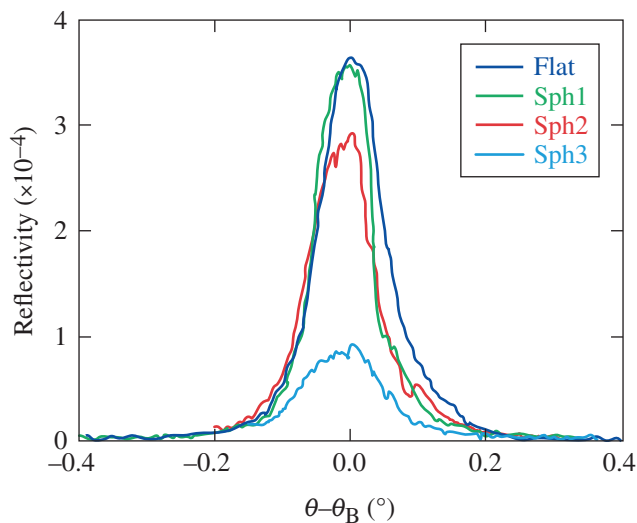


Figure 136.8

Measured rocking curves of four quartz crystals (234) at 15.6909 keV. The spherical crystal Sph1 had a peak reflectivity of $(3.6 \pm 0.7) \times 10^{-4}$ and a rocking-curve full width at half maximum of 0.09° . Also shown are the rocking curves for another spherical crystal (Sph2) and a flat crystal, all from the same production batch, and a third spherical crystal (Sph3) obtained from a different vendor.

The theoretical value of reflectivity for each crystal was calculated using the x-ray oriented programs (*XOP*) code.¹² The *XOP* code uses the *DEBAX* database of atomic and molecular properties and photon-interaction cross sections and scattering factors for a wide range of crystal materials. The crystal type was selected to be α quartz with the Miller indices set to (468), indicating that the calculation was performed for the second-order diffraction. The photon energy was set to 15.69 keV, the Poisson ratio to 0.17, and the polarization to sigma. The asymmetry angle was set to 0° , signifying perfect parallelism between the diffracting planes and the crystal surface. The diffraction geometry was set to Bragg and, to account for the crystal curvature, the calculation theory was set to Multilamellar. The final input parameter was the Debye–Waller temperature parameter that took into account the thermal motion of the crystal lattice. The precise value of the temperature parameter is difficult to determine for trigonal crystalline structures such as quartz. Approximate formulas exist in *XOP* for cubic crystal structures such as pure silicon. In that case, the temperature parameter is close to unity for the lowest-order diffraction but is reduced for higher orders. In the current calculation, the tem-

perature factor was a free parameter that was adjusted until the calculated width of the rocking curve matched the experimentally observed value. The corresponding reflectivity values were then recorded. The temperature parameter and the calculated peak and integrated reflectivity for spherical crystals Sph1 and Sph3 are displayed in Table 136.II. The calculated values of the integrated reflectivity for the two crystals are a factor of ~ 3 and ~ 8 higher than the measured values, respectively.

It is not clear why the measured reflectivity is lower than the predicted values. Measurements of the crystal thickness of Sph1 indicated that the thickness was within 2% of the stated value. The calculations include x-ray absorption in quartz, which for a 71- μm thickness decreases the calculated reflectivity by $\sim 9\%$ compared to the case where absorption is not included. Absorption by impurities is not accounted for but is an unlikely explanation; although moderate- to high- Z impurities could have a significant effect on absorption, the most-common impurities in quartz crystals are low- Z materials such as Li and Al, and since the crystal is visibly transparent, we can assume that the crystal is reasonably pure. Another possibility is that the reflectivity was suppressed by defects introduced in the crystal during the manufacturing process. We also cannot eliminate the possibility that imperfections on the substrate surface might have been transferred to the crystal or that the bonding mechanism introduced stress and dislocations to the diffracting structures. There is no indication that the additional bending of the crystal led to any further degradation since the reflectivity of the flat sample was similar in magnitude to the curved crystals. Finally, the application of models that are strictly derived for cubic crystal geometry provides uncertainty and another potential source of disagreement between the measured and calculated values.

Imaging Capability and Reflectivity Using a Plasma-Based Source

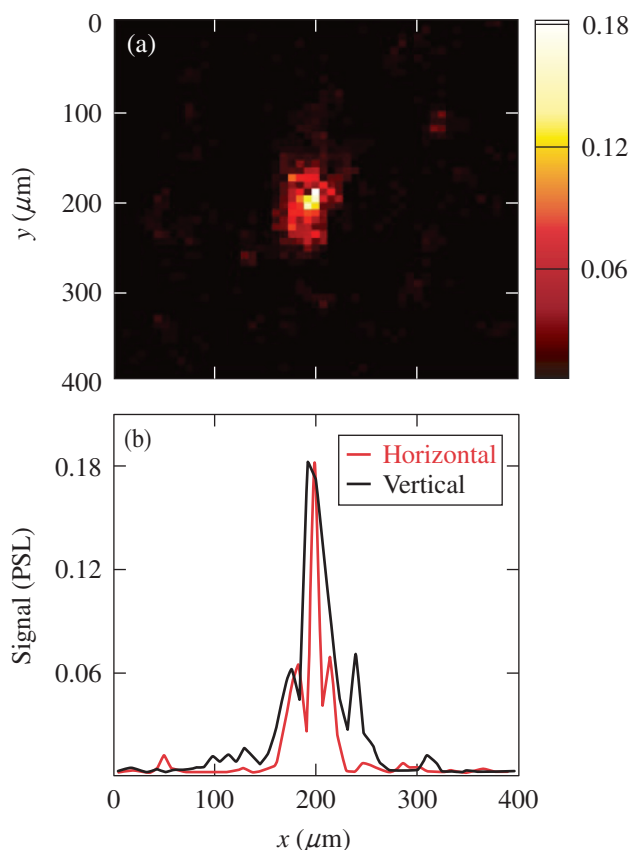
Laser experiments were performed with LLE's Multi-Terawatt (MTW) laser¹³ to test the imaging capability of a spherical crystal using Zr $K_{\alpha 2}$ x rays. This test was performed with the sample Sph3. The crystal imaged the emission from

the rear surface of a Zr foil target irradiated with a p -polarized laser pulse with a 10-J energy incident at a 45° angle. The laser energy is absorbed by electrons at the critical-density surface of a plasma that forms in front of the target at the beginning of the laser interaction. The electrons are driven into the target where they stimulate the emission of K_{α} radiation. The K_{α} yield from such a target is proportional to the laser energy, while background noise caused by bremsstrahlung as the electrons lose energy in collisions is proportional to the laser intensity. To reduce the background, the pulse duration was lengthened to 10 ps and the laser spot was defocused to $\sim 30 \mu\text{m}$ (FWHM) corresponding to a mean intensity of $\sim 1 \times 10^{17} \text{ W/cm}^2$. The crystal was oriented to reflect the $K_{\alpha 2}$ emission on a Fujifilm TR imaging plate. To further reduce the background signal and enhance the signal-to-background ratio, a 17- μm -thick Zr filter and a 25- μm -thick Al filter were placed in front of the imaging plate while a 3-mm-thick lead collimator obstructed the direct line of sight to the target. The target dimensions were 1 mm \times 1 mm \times 17 μm . The distance from the target to the center of the crystal was 28.9 cm, providing a magnification of 6.6. The crystal diameter was 2.5 cm, corresponding to a solid angle from the target of 5.9×10^{-3} sr. The extreme rays that diffract at the edge range of the crystal subtend angles of 2.2° and 4.4° . The corresponding energies were 15.679 keV and 15.711 keV, respectively, giving an energy acceptance bandwidth for the crystal of 32 eV. The $K_{\alpha 2}$ line broadening and shifting that accompany target heating are not expected to be significant for the current case of moderate laser energy and a large-mass target, and the $K_{\alpha 2}$ line is expected to remain fully within the bandwidth.

Figure 136.9 shows an image corrected for magnification along with a horizontal and a vertical lineout through the peak intensity pixel. The FWHM of the horizontal and vertical lineouts is 32 and 38 μm , respectively. The image exhibits a signal-to-background ratio of better than 40:1 with an x-ray signal that peaks at around 0.18 PSL. A single-photon-counting spectrometer¹⁴ determined the total number of radiated K_{α} photons to be $(10^{+7/-2}) \times 10^{10}$ corresponding to a laser-to- K_{α} energy conversion efficiency of $\sim 3 \times 10^{-5}$. Taking into

Table 136.II: The peak and integrated reflectivity for each crystal calculated using the x-ray oriented programs (XOP) software.¹²

Crystal	Radius of curvature (cm)	Thickness (μm)	Temperature parameter	Peak reflectivity	Integrated reflectivity (mrad)
Sph1	50	71	0.45	1.4×10^{-3}	2.2×10^{-3}
Sph3	50	125	0.35	1.0×10^{-3}	2.1×10^{-3}



E21816JR

Figure 136.9

(a) An image of the Zr $K_{\alpha 2}$ emission through the rear surface of a 17- μm -thick laser-irradiated Zr foil (the color scheme refers to the measured signal in PSL) and (b) horizontal and vertical lineouts through the peak of the emission.

account the relative solid angle between the single-photon-counting spectrometer and the crystal, the total number of K_{α} photons incident on the quartz crystal was $\sim 5 \times 10^7$. The quartz crystal reflects only the $K_{\alpha 2}$ line on the detector, which contains one third ($\sim 1.6 \times 10^7$) of the total number of K_{α} photons. Accounting for the 17- μm -thick Zr filter and the 25- μm -thick Al filter ($\sim 77\%$ total transmission) and assuming an imaging plate sensitivity of (2.5 ± 0.5) mPSL/photon at 15.7 keV (Ref. 15), a perfectly reflecting crystal is estimated to produce a total signal of $(3.0 + 3.4/-1.1) \times 10^4$ PSL. Comparing this with the experimentally measured value of (5.5 ± 1.1) PSL, which is the spatially integrated value from Fig. 136.9, implies a peak reflectivity of $(1.8 + 1.4/-1.0) \times 10^{-4}$ at 15.7 keV. The peak reflectivity inferred from the laser experiment is a factor of ~ 2 higher, but it is within the experimental uncertainties in reasonable agreement with the peak reflectivity obtained from the rocking curve measurement of Sph3 (see Table 136.I).

Conclusion

A high-energy x-ray-photon imager has been developed to image the x-ray emission from laser-generated Zr plasmas. The imager's optic consists of a spherically bent quartz crystal with Miller indices (234) and a focal length of 25 cm. The Bragg angle, rocking curve, and reflectivity were determined for three spherically bent samples. A flat crystal was tested as a control to determine the impact of the bending procedure. The experiments were carried out at The National Synchrotron Light Source using photons with an energy of 15.6909 keV, corresponding to the Zr $K_{\alpha 2}$ line. The lattice $2d$ spacing for two of the curved samples was determined by the supplier to be $2d = 1.5827(7)$ Å, corresponding to Bragg and incidence angles, for Zr $K_{\alpha 2}$ x rays of $(86.8 \pm 0.5)^\circ$ and $(3.2 \pm 0.5)^\circ$, respectively. The incident angle of the third curved sample was directly measured to be $(2.8 \pm 0.3)^\circ$, resulting in a Bragg angle of $(87.2 \pm 0.3)^\circ$ and inferred $2d = 1.5822(4)$ Å. The peak reflectivity and rocking curve width for the best-performing sample were determined to be $\sim 4 \times 10^{-4}$ and $\sim 0.1^\circ$, respectively. An image of the Zr line emission was obtained using a laser-generated Zr plasma produced by the 10-J Multi-Terawatt laser. The measurement confirmed the peak reflectivity of the crystal for the Zr $K_{\alpha 2}$ line by using the emitted K_{α} photon number measured with an absolutely calibrated single-photon-counting spectrometer.¹⁴

ACKNOWLEDGMENT

This work was supported by the U.S. Department of Energy Office of Inertial Confinement Fusion under Cooperative Agreement No. DE-FC52-08NA28302, the University of Rochester, and the New York State Energy Research and Development Authority. This work was also supported by the U.S. Department of Energy Office of Fusion Energy Sciences (OFES), Fusion Science Center grant No. DE-FC02-04ER54789, the OFES ACE Fast Ignition grant No. DE-FG02-05ER54839, the Office of Basic Energy Sciences under contract No. DE-AC02-98CH10886, and Brookhaven National Laboratory under LDRD 05-057. The support of DOE does not constitute an endorsement by DOE of the views expressed in this article.

REFERENCES

1. M. Tabak *et al.*, Phys. Plasmas **1**, 1626 (1994).
2. W. Theobald, A. A. Solodov, C. Stoeckl, K. S. Anderson, R. Betti, T. R. Boehly, R. S. Craxton, J. A. Delettrez, C. Dorrer, J. A. Frenje, V. Yu. Glebov, H. Habara, K. A. Tanaka, J. P. Knauer, R. Lauck, F. J. Marshall, K. L. Marshall, D. D. Meyerhofer, P. M. Nilson, P. K. Patel, H. Chen, T. C. Sangster, W. Seka, N. Sinenian, T. Ma, F. N. Beg, E. Giraldez, and R. B. Stephens, Phys. Plasmas **18**, 056305 (2011).
3. T. R. Boehly, D. L. Brown, R. S. Craxton, R. L. Keck, J. P. Knauer, J. H. Kelly, T. J. Kessler, S. A. Kumpan, S. J. Loucks, S. A. Letzring, F. J. Marshall, R. L. McCrory, S. F. B. Morse, W. Seka, J. M. Soures, and C. P. Verdon, Opt. Commun. **133**, 495 (1997).

4. R. B. Stephens *et al.*, Phys. Rev. E **69**, 066414 (2004).
5. M. H. Key, J. C. Adam, K. U. Akli, M. Borghesi, M. H. Chen, R. G. Evans, R. R. Freeman, H. Habara, S. P. Hatchett, J. M. Hill, A. Heron, J. A. King, R. Kodama, K. L. Lancaster, A. J. MacKinnon, P. Patel, T. Phillips, L. Romagnani, R. A. Snavely, R. Stephens, C. Stoeckl, R. Town, Y. Toyama, B. Zhang, M. Zepf, and P. A. Norreys, Phys. Plasmas **15**, 022701 (2008).
6. L. Jarrott, M. S. Wei, H. Sawada, W. Theobald, A. A. Solodov, C. McGuffey, R. B. Stephens, C. Stoeckl, C. Mileham, F. Marshall, J. Delettrez, R. Betti, P. K. Patel, H. McLean, C. Chen, M. H. Key, T. Doeppner, T. Yabuuchi, T. Iwawaki, H. Habara, A. Greenwood, N. Alfonso, D. Hoover, E. Giraldez, and F. N. Beg, Bull. Am. Phys. Soc. **57**, 115 (2012).
7. W. Theobald, A. A. Solodov, C. Stoeckl, V. Yu. Glebov, S. Ivancic, F. J. Marshall, G. McKiernan, C. Mileham, T. C. Sangster, F. N. Beg, C. Jarrott, E. Giraldez, R. B. Stephens, M. S. Wei, M. H. Key, H. McLean, and J. Santos, Bull. Am. Phys. Soc. **57**, 115 (2012).
8. U. K. Akli, "Fast Ignition Experimental and Theoretical Studies," Ph.D. thesis, University of California at Davis, 2006.
9. J. Delettrez, R. Epstein, M. C. Richardson, P. A. Jaanimagi, and B. L. Henke, Phys. Rev. A **36**, 3926 (1987).
10. K. U. Akli, M. S. del Rio, S. Jiang, M. S. Storm, A. Krygier, R. B. Stephens, N. R. Pereira, E. O. Baronova, W. Theobald, Y. Ping, H. S. McLean, P. K. Patel, M. H. Key, and R. R. Freeman, Rev. Sci. Instrum. **82**, 123503 (2011).
11. Z. Zhong *et al.*, Nucl. Instrum. Methods Phys. Res. A **450**, 556 (2000).
12. M. Sanchez del Rio and R. J. Dejus, in *Advances in Computational Methods for X-Ray and Neutron Optics*, edited by M. Sanchez del Rio (SPIE, Bellingham, WA, 2004), Vol. 5536, pp. 171–174.
13. V. Bagnoud, I. A. Begishev, M. J. Guardalben, J. Puth, and J. D. Zuegel, Opt. Lett. **30**, 1843 (2005).
14. B. R. Maddox *et al.*, Rev. Sci. Instrum. **79**, 10E924 (2008).
15. A. L. Meadowcroft, C. D. Bentley, and E. N. Stott, Rev. Sci. Instrum. **79**, 113102 (2008).